Article

Acoustic Compressibility of *Caenorhabditis elegans*

Thierry Baasch,[1] Peter Reichert,[1,*] Stefan Lakämper,[1] Nadia Vertti-Quintero,[2] Gamuret Hack,[1] Xavier Casadevall i Solvas,[2] Andrew deMello,[2] Rudiyanto Gunawan,[2,3] and Jürg Dual[1]

[1]Institute for Mechanical Systems, Department of Mechanical and Process Engineering and [2]Institute for Chemical and Bioengineering, Department of Chemistry and Applied Biosciences, Swiss Federal Institute of Technology, ETH Zurich, Zurich, Switzerland; and [3]Swiss Institute of Bioinformatics, Lausanne, Switzerland

ABSTRACT The acoustic compressibility of *Caenorhabditis elegans* is a necessary parameter for further understanding the underlying physics of acoustic manipulation techniques of this widely used model organism in biological sciences. In this work, numerical simulations were combined with experimental trajectory velocimetry of L1 *C. elegans* larvae to estimate the acoustic compressibility of *C. elegans*. A method based on bulk acoustic wave acoustophoresis was used for trajectory velocimetry experiments in a microfluidic channel. The model-based data analysis took into account the different sizes and shapes of L1 *C. elegans* larvae ($255 \pm 26 \ \mu$m in length and $15 \pm 2 \ \mu$m in diameter). Moreover, the top and bottom walls of the microfluidic channel were considered in the hydrodynamic drag coefficient calculations, for both the *C. elegans* and the calibration particles. The hydrodynamic interaction between the specimen and the channel walls was further minimized by acoustically levitating the *C. elegans* and the particles to the middle of the measurement channel. Our data suggest an acoustic compressibility κ_{Ce} of 430 TPa^{-1} with an uncertainty range of ± 20 TPa^{-1} for *C. elegans*, a much lower value than what was previously reported for adult *C. elegans* using static methods. Our estimated compressibility is consistent with the relative volume fraction of lipids and proteins that would mainly make up for the body of *C. elegans*. This work is a departing point for practical engineering and design criteria for integrated acoustofluidic devices for biological applications.

INTRODUCTION

The precise manipulation of micrometer-sized objects in solution such as droplets, particles, and, more importantly, cells, cell-aggregates, and small organisms is of great interest in modern biology. An increasing need for compact and low-cost manipulation solutions has driven the development of both microfluidic lab-on-a-chip devices and a number of noncontact methods (1,2).

Previous acoustophoretic work on living organisms has focused mostly on immotile specimens such as unflagellated bacteria, yeast, and isolated or aggregated mammalian cells (3,4). The direction and speed of acoustophoresis are determined by the compressibility κ and density ρ of the specimen and its surrounding medium. In this context, the term "compressibility" (κ) refers specifically to the acoustic compressibility at high frequencies, i.e., in highly dynamic conditions. For most spherical biological specimen, like single cells or cell aggregates in standard buffers, relatively

high acoustic energies are often needed to move a specimen toward a pressure node at a given velocity, compared to, for example, a silica microsphere in the same buffer. Relatively high acoustic energies are also needed to manipulate motile single-celled organisms such as the algae Euglena and salmonella, which could be focused in acoustic standing waves (5–7). For these reasons, an accurate determination of the compressibility κ is important not only for the prediction and estimation of the acoustic mobility, but also for elucidating the biophysical properties and cellular composition of a specimen.

C. elegans is a widely used animal model for studying fundamental biological processes at a multicellular organism level and is receiving increased attention also in the context of microfluidics (8,9). Despite its wide implications for biological and biomedical research, acoustic manipulation of *C. elegans* has only been attempted recently (10–12). Although experimental measurements of the *C. elegans* density exist (13), a characterization of its acoustic compressibility at high frequencies in the MHz range is not yet available. The knowledge of this parameter is crucial for experimentation using acoustophoresis on this model organism. Although a recent study reported the

compressibility value for *C. elegans* (14), this value was obtained by observing the response of *C. elegans* to static pressure changes. Thus, the outcome might be relevant for bulk behavior of *C. elegans* with defects in osmoregulation. The compressibility values $\kappa_{Ce,S} = (625–833) \times 10^4$ TPa^{-1} obtained in a static setting are not per se transferable to the highly dynamic acoustic settings (14).

Here, we present the first, to our knowledge, measurement of the acoustic compressibility of *C. elegans*. We used a standard particle trajectory velocimetry (PTV)-based method (15) to determine the pressure field inside our bulk acoustic wave (BAW) device. We also performed worm trajectory velocimetry (WTV). The data of the WTV, together with the pressure field, were employed to determine *C. elegans* compressibility. To minimize the influence of the channel walls on the hydrodynamic drag of the specimen, the worms and particles were levitated acoustically between top and bottom channel walls. Furthermore, the channel walls were taken into account in the calculation of the drag coefficients. Numerical scattering simulations were carried out by taking into account the characteristic nonspherical shape of the *C. elegans* to produce a calibration curve relating the compressibility of the *C. elegans* to experimentally determined trajectories. For this purpose, we introduced a simplified and numerically efficient simulation procedure based on a strategy previously established for erythrocytes or disks (16). Finally, the compressibility of *C. elegans* was obtained by minimizing the difference between the simulated and experimentally observed worm velocity from the WTV data.

METHODS

C. elegans maintenance, treatment and density

In our experiments, we employed N2 wild-type *C. elegans* obtained from the Caenorhabditis Genetics Center of the University of Minnesota (Minneapolis, MN). Standard protocols to maintain *C. elegans* were applied (17). *C. elegans* populations were obtained by seeding NGM/*Escherichia coli* (OP50) plates with arrested larvae. After 72 h at 20°C gravid, adults were washed out from the plates with M9 buffer and transferred to a tube in which they were allowed to form a pellet under gravity. These pellets were transferred into fresh NGM/OP50 plates, where *C. elegans* were subsequently bleached using a 50/50% solution of 1 M NaOH and hypochlorite. The resulting synchronized populations were kept sufficiently fed at 20°C until a desired stage of larvae was reached. *C. elegans* were washed out of the NGM plates for further experiments using M9 buffer, 20 h after egg hatching, ensuring L1 larvae with a length of ∼250 μm (18). All *C. elegans* were collected in M9-buffer (approx. 5 mL M9 per plate) and the samples were then diluted to appropriate densities of *C. elegans*. We immobilized (paralyzed) the *C. elegans* by treating them with 100 mM Levamisole for 5 min (10) (Supporting Materials and Methods, Section 1) such that we could approximate the *C. elegans* geometry in the finite element model using a rod-like structure.

The density of *C. elegans* ρ_{Ce} has been previously reported in the literature by Reina et al. (13) for multiple stages of development and starvation, with values ranging from 1040 to 1090 kg/m^3. In this work, we measured the density of the L1 *C. elegans* ρ_{Ce} to be between 1070 and 1080 kg/m^3 and assumed a reference density of 1075 ± 5 kg/m^3 (Supporting Materials and Methods, Section 2).

In this work, the *C. elegans* were synchronized in size (length of ∼250 μm). The corresponding age varies between the early L1 stage and the late L1 stage just before the L1/L2 molt. Even though the size variation of our used *C. elegans* is small, it is possible that an internal morphology variation is present. The variations in ex utero development could be compensated if we used L1 arrested stage worms (19). We decided against the use of the L1 arrested stage as Reina et al. (13) investigated a significant density change for adult worms under starvation stress.

Device and observation setup

The device and observation principles are schematically depicted in Fig. 1. The device production techniques are described in detail by Gatzen et al. (20). Briefly, microfluidic channels with straight channel walls were dry-etched 86 μm deep in a silicon wafer (500 μm thick) by the so-called
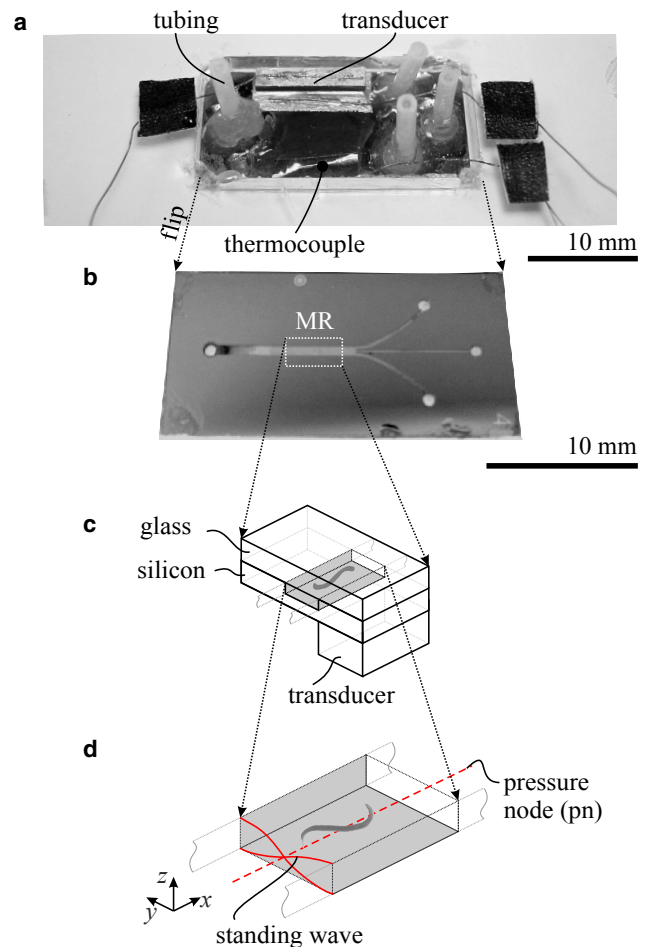

FIGURE 1 Manipulation device and setup. (*a*) A photograph of the back side of the device glued to a polymethacrylate holder, with fluid inlet and outlet tubing. The piezoelectric transducer used to excite the acoustic standing wave is glued to the silicon surface, and a thermocouple allows the monitoring of the temperature. (*b*) A photograph of the front side of the device showing the microfluidic channel design. The dotted rectangle marks the measurement region (MR) for data acquisition. (*c*) A schematic cross-section of the layered micro-fabricated structure with glass and silicon layers, which enclose the fluidic manipulation channel. (*d*) An illustration of one *C. elegans* exposed to an acoustic standing wave in the manipulation channel. The λ/2-mode is sketched in solid red. The resulting pressure nodal line is indicated by the red dashed line.

"Bosch process" using an inductively coupled plasma system. The channels were placed in the center of the 24 × 12 mm device. We set the channel dimensions to be $l \times w \times h = 12,000 \times 700 \times 86 \; \mu m$ (see Fig. 1 *b*; (21)).

The wafer front side was covered by a glass wafer (500 μm thick), which was anodically bonded to the silicon substrate. Access to the inlet and outlets was provided by dry-etching from the back side of the silicon wafer. Short Teflon tubes (10 mm length, 0.75 mm inner diameter) were flanged with the Easy-Flange kit (Cetoni, Korbußen, Germany) and glued with instant adhesive and epoxy adhesive onto the inlet and outlets to allow subsequent attachment of similar Teflon-tubing connecting syringes or reservoirs. The device was finally mounted on a polymethacrylat holder (microscopy slide size, 75 × 25 mm) (Fig. 1 *a*).

To monitor the temperature inside the device, a thermocouple was attached at a distance of ∼4 mm to the channel onto a highly thermally conductive silicon and covered with a Kapton tape (Fig. 1 *a*).

A piezoelectric transducer (PZ26; Ferroperm Piezoceramics, Kvistgård, Denmark) (size $l \times w \times h = 10 \times 2 \times 1$ mm) was glued with conductive epoxy (H20E; Epoxy Technology, Billerica, MA) in parallel direction to the channel (at a distance of 4 mm) on the back side of the silicon chip, as shown in Fig. 1 *c*. The piezo was wired using instant adhesive and conductive silver paste. For electrical excitation, the top and bottom electrodes of the piezoelectric transducer were connected to a function generator (AFG 3022B; Tektronix, Beaverton, OR) and a power amplifier (2100L; ENI, Rochester, NY) with a 50 Ω termination. Applied excitation voltages in the *C. elegans* experiments were 19.5 Vpp (voltage peak-to-peak) for 0.97 MHz, 27 Vpp for 2.165 MHz and 22.3 Vpp for 7.995 MHz. The frequencies were chosen to excite resonance modes and achieve high pressure amplitudes in the water channel. The piezoelectric transducer converted the applied electrical input in a mechanical vibration for the excitation of standing pressure waves inside the microfluidic channel, as illustrated in Fig. 1 *d*.

Yeast, particle, and WTV experiments were imaged using a high-speed camera (HiSpec 1 Mono; Fastec Imaging, San Diego, CA) and a bright-field microscope (12× UltraZoom; Navitar, Rochester, NY for Fig. 2 *b* and LSM 5 Pascal, LD Plan-Neofluar 20×/0.4 Corr Ph2 objective; Zeiss, Oberkochen, Deutschland, Germany for Fig. 2 *c*). The high reflectivity of silicon created a bright illumination for high-speed recordings. A LabView program was used to control the function generator output, record temperature readings of the thermocouple, and trigger the high-speed camera recording.

The acoustic experiments were performed at an ambient temperature of 25°C. The temperature beneath the microscope was controlled with a feedback loop consisting of a Pt100 temperature sensor next to the device, a Peltier element or fan unit (AA-019-12-22-00-00; Laird Technologies, Chesterfield, MO) and a Peltier controller (TC2812-RS232; CoolTronic, Beinwil am See, Switzerland). At the highest applied driving amplitude, the device heated up to a maximum of 27°C (see Supporting Materials and Methods, Section 3).

Theoretical development

In BAW acoustophoresis, the device has to be fabricated out of materials with a high acoustic impedance contrast to the fluid, in most cases silicon or glass, to reach sharp acoustic resonances in the fluid cavity. Typical operating resonance frequencies are chosen such that a standing wave is formed in the channel width. Consider acoustic resonances in a rectangular fluid chamber of length l, width w, and height h. We assume a one-dimensional standing wave in the channel width y-direction. If the zero of the coordinate system is set in the channel middle then the assumed pressure profile as a function of position y and time t is given by (Fig. 1 *d*):

$$p(y, t) = p_a \cos\left[k\left(y + \frac{w}{2}\right)\right]\cos(\omega t), \quad (1)$$

where p_a denotes the pressure amplitude, ω is the angular frequency, $k = 2\pi/\lambda$ denotes the wavenumber, λ the wavelength and the coordinate
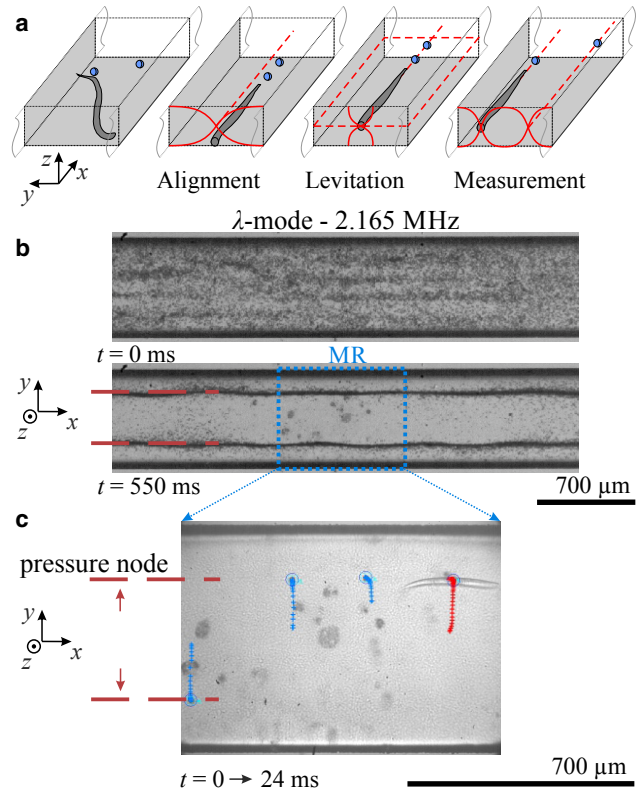

FIGURE 2 Overview of the PTV and WTV procedure. (*a*) A three-dimensional illustration of the three steps of the WTV and PTV procedure. First, the specimens are brought to the $y = 0$ plane and are aligned with respect to the channel length. Then they are levitated against gravity and focused in the channel middle line ($y = 0$, $z = 0$). Finally, for the trajectory measurement, the levitation in z-direction is turned off and the field in y-direction is switched from the $\lambda/2$-mode to the λ-mode. (*b*) Acoustic alignment of levitated yeast cells along the pressure nodal lines (marked by *red dashes*) in water (Video S1). The blue rectangle indicates the measurement region (MR), used for both *C. elegans* and device characterization experiments. (*c*) PTV and WTV example within the MR for a distribution of polystyrene particles with a diameter of 15.59 μm and one L1 *C. elegans* suspended in buffer (Video S2). The tracking data points are shown in blue for individual particles and in red for the *C. elegans*.

system is centered in the channel. This assumption is commonly taken in the literature and has been recently validated experimentally by Lamprecht et al. (22,23). This function can be determined analytically up to the pressure amplitude p_a, which is the single unknown parameter. Here, we estimated p_a using data from the PTV (see Numerical Methods). In the context of this work, we further neglected any contributions from the acoustic streaming. For small particles with a radius smaller than 1 μm, the streaming forces may become important. However, because the L1 *C. elegans* in our experiments had diameters larger than 10 μm, their motion should be predominantly controlled by the acoustic radiation forces.

Given the above approximation, the time averaged acoustic radiation force F_{ac} acting on small spherical particles (radius r, $r << \lambda$) in inviscid fluid for a one-dimensional acoustic standing wave, can be written analytically as follows (24,25):

$$F_{ac} = 4\pi r^3 \Phi(\overline{\kappa}, \overline{\rho})k E_{ac} \sin\left[2k\left(y + \frac{w}{2}\right)\right], \quad (2)$$

where $E_{ac} = p_a^2/4\rho_w c_w^2$ denotes the acoustic energy for a standing wave, $\Phi(\overline{\kappa}, \overline{\rho}) = 1/3[(5\overline{\rho} - 2/2\overline{\rho} + 1) - \overline{\kappa}]$ is the so-called acoustic contrast factor with $\overline{\rho} > (\rho_p/\rho_w)$ and $\overline{\kappa} > (\kappa_p/\kappa_w)$ denoting the relative density and the relative compressibility, respectively. In the equation above, the subscripts p and w denote the material parameters of the particle and water, respectively.

Using the *C. elegans* diameter as characteristic length and a velocity of 0.015 m/s, which we determined experimentally, as their characteristic velocity, we obtain a Reynolds number in the order of 0.2. In this regime of small Reynolds number, the error applying the Stokes' drag approximation is considered small (26,27). Additionally, we neglected the inertial forces of the *C. elegans*, which is in line with the methodology of Barnkob (28). Assuming Stokes' flow and neglecting the inertial forces, the trajectory of an isolated spherical particle moving in a sound field can be calculated analytically by balancing the acoustic radiation force with the Stokes' drag (15). To consider the effect of the top and bottom channel walls on the hydrodynamic drag coefficient, we used the correction factor found by Faxén (29) (see Supporting Materials and Methods, Section 4).

Because the hydrodynamic and acoustic forces depend on the shape of the particles, a different formulation has to be used for *C. elegans*. We approximated the immobilized *C. elegans* in our study as a straight cylinder with a fixed geometry. The cylinder was parametrized using the diameter and length, which were measured in the experiments. An analytical solution for the hydrodynamic drag force acting on a cylinder between two parallel walls has been described by De Mestre (30) (see Supporting Materials and Methods, Section 4). For *C. elegans*, the acoustic scattering problem for the calculation of the acoustic radiation force can be significantly simplified by assuming 1) a one-dimensional wave-field; 2) that the viscous boundary layer given by $\delta_v = (2\eta_w/\rho_w \omega)^{0.5} \approx 0.5$ μm, where η_w and ω denote the dynamic viscosity and angular frequency, respectively, is much smaller than the diameter of the *C. elegans* $d_{Ce} \approx 15$ μm (L1 larvae), and thus the fluid can be considered as inviscid; 3) that, provided a purely translational motion, the acoustic radiation force on *C. elegans* scales with respect to the pressure amplitude, wavelength, and wave-field geometry, in the same manner as the acoustic radiation force on spherical objects. Further, we assumed constant relative density ratio ρ_{Ce}/ρ_w and compressibility of water κ_w, i.e., the effect of temperature variation on these parameters is negligible. In our numerical simulations, we used κ_w of 444 TPa^{-1}, ρ_w of 1000 kg/m^3 and *C. elegans* density ρ_{Ce} of 1075 kg/m^3. Considering the aforementioned assumptions, the time-averaged acoustic radiation force acting on *C. elegans* can be formulated as:

$$F_{ac} = \frac{f(G, \kappa_{Ce})}{\lambda} p_a^2 \sin\left[2k\left(y + \frac{w}{2}\right)\right], \quad (3)$$

where the function f depends on the material parameters of the fluid and worm and on the worm geometry G (diameter and length). Because the carrier fluid is always water, its parameters are omitted in the following. By using a linear approximation f_{lin} of $f(G, \kappa_{Ce})$ for a given geometry G:

$$f \approx f_{lin} = d\kappa_{Ce} + e, \quad (4)$$

the acoustic radiation force on worms can readily be evaluated up to two unknown constant parameters e and d. These two coefficients depend on the geometry (length and diameter) and density of the *C. elegans* and the material properties of the fluid. In the case of a small spherical particle, the coefficient d is constant and e is proportional to $(5\overline{\rho} - 2/2\overline{\rho} + 1)$ multiplied by the water compressibility κ_w (see Supporting Materials and Methods, Section 5). Please note that the parameters d and e change when a different medium or *C. elegans* density is assumed. Thus, instead of calculating the acoustic radiation force at every time-step, it is possible to estimate these constant geometrical correction factors numerically. This can be done by calculating the acoustic radiation force for multiple values of pressure amplitude, wavelength and *C. elegans* compressibility, and fitting the parameters d and e to the simulation results. To calculate the acoustic radiation force acting on the *C. elegans* we used COMSOL (Comsol A/S, Lyngby, Denmark) in combination with the method presented by Hahn et al. (16).

Device characterization and data acquisition for PTV and WTV

As illustrated in Fig. 1, we performed PTV and WTV simultaneously in our BAW device. The PTV provides data for the determination of pressure amplitude following the work of Barnkob et al. (28,31). To calculate the drag force for both particles and *C. elegans*, the position in the measurement channel has to be defined in three dimensions. We applied the measurement procedure presented in Fig. 2 *a* for both PTV and WTV experiments with the possibility of alignment in *x*-/*y*-direction and a levitation in *z*-direction. Briefly, *C. elegans* and particles were injected into the microfluidic chamber where they settled at the bottom of the channel in a random orientation. A half wavelength standing wave (λ/2-mode) in *y*-direction at 0.97 MHz was used to align *C. elegans* and particles. A λ/2-mode in *z*-direction at 7.995 MHz levitated the aligned *C. elegans* and particles, lifting them against the gravitational forces and positioning them between channel top and bottom. This step minimized the influence of the channel walls on the hydrodynamic drag of the specimen. The levitated and aligned position in the channel middle was the starting position for all PTV and WTV experiments. Then the 7.995 MHz actuation was turned off and the actuation was switched to the full wavelength λ-mode at 2.165 MHz, inducing the translation of the particles and *C. elegans* from the channel middle to the channel sides. During the complete procedure of switching the modes and translating the specimen, the total theoretically estimated sedimentation distance was ~10 μm in the *z*-direction, which is sufficiently small compared to the channel height. Details on the mode switching procedure are given in Supporting Materials and Methods, Section 6. The resulting trajectories of the particles and worms were recorded and used for the determination of the pressure amplitude and the *C. elegans* compressibility, respectively.

The λ-mode standing wave could be visualized using a yeast cell suspension (*Saccharomyces cerevisiae*), as shown in Fig. 2 *b* (Video S1). Most yeast cells were levitated and moved to the nodal lines of the λ-mode in 100 ms. Yeast cells, like most biological material in watery solutions, have a positive acoustic contrast factor and were thus driven to the pressure nodal lines. The time duration of 550 ms was sufficient for all yeast cells to align with the respective nodal line. A homogeneous distribution of yeast cells along the pressure nodal lines in the measurement region (MR) could be observed. If there was a pressure variation along the channel length, then the yeast cells would not form a connected line but disconnected clumps. The observed yeast cell distribution gives a strong support for the validity of our one-dimensional pressure field assumption. Thus, Eq. 2 is suitable to describe forces on spherical particles inside our acoustic field.

An example of simultaneous particle and *C. elegans* tracking is depicted in Fig. 2 *c*. The MR had a length of 1 mm. For PTV experiments, we used highly uniform standard polystyrene micro-spheres (PS-F-15.6; microParticles, Berlin, Germany, mean diameter 15.59 μm, SD 0.13 μm, 0.8% coefficient of variation, information as provided by supplier and acoustic contrast factor of Φ=0.1619). The properties of the microspheres can be found in Supporting Materials and Methods, Section 7. The particle temporal position (trajectory) was extracted from high-speed image sequences using a toolbox implemented in MATLAB (The MathWorks, Natick, MA) (see Fig. 2 *c*; Video S2; (32)). Subsequently, we used a least-square estimation to obtain the pressure amplitude by fitting the total acoustic force given in Eq. 2 using known properties of the particles (radius, density, compressibility) and the buffer to the particle trajectories. As the pressure amplitude varied slightly along the channel *x*-direction, we measured the particle velocities at multiple positions along the channel and interpolated the pressure amplitudes linearly.

In WTV experiments, we acquired high-speed imaging data of the acoustic mobility of Levamisole-treated *C. elegans* (described in C. elegans Maintenance, Treatment and Density). The *C. elegans* adopted an almost ideal rod-like shape, which enabled efficient data acquisition and analysis and, more importantly, justified the finite element model describing *C. elegans* acoustic trajectories. Here, the feature tracking of *C. elegans*

was performed with a semiautomated video analysis software (ProAnalyst; Xcitex, Woburn, MA).

We analyzed the *C. elegans* traces for which the *C. elegans* did not change its orientation, such that our simplification of a one-dimensional pressure distribution is valid. More specifically, we ensured that the tracking point at the mid-axis of the *C. elegans* translated only along the *y*-axis. The *C. elegans* position in the channel *z*-plane was monitored with the microscope focus. The dimension of each *C. elegans* was measured and the *C. elegans* geometry was recorded to be used in the model simulation.

Defining the origin at the respective nodal line to be reached, the worm positional data were taken between 140 and 70 μm. We defined an indicator velocity v_{ind} according to (see Fig. 4 *a*):

$$v_{ind} = \frac{(140 - 70)\ \mu m}{t_{70} - t_{140}} = \frac{\Delta y}{\Delta t}, \qquad (5)$$

where t_d indicates the time a worm is a distance of d μm away from the closest pressure nodal line. Note that v_{ind} adopts only positive values. The indicator velocity v_{ind} can be seen as the averaged velocity of a worm moving from 140 to 70 μm toward the pressure node. We also performed the simulations with other choices for the start points and endpoints of the indicator velocity. In theory, the choices should yield identical compressibility estimates. However, the choice of the segment when determining the indicator velocity resulted in an uncertainty of ± 3 TPa^{-1}.

Numerical methods

The estimation of *C. elegans* compressibility is based on minimizing the difference between the simulated worm velocity $v_{ind,s}$ predicted by simulating the worm trajectory $y_{k,s}$ for a given value of κ_{Ce},s and the experimental worm velocity $v_{ind,e}$ from WTV experiments as described in Eq. 5. The whole procedure is explained in the flow chart shown in Fig. 3. First, we computed the Stokes' drag acting on a *C. elegans* between two parallel channel walls using an analytical formulation from the slender body theory (Fig. 3 *a*). To simplify and speed up the acoustic radiation force calculations, we numerically determined the geometry factors d and e for the linearized function f_{lin}, as described in Eq. 4 (Fig. 3 *b*). More specifically, for a given worm geometry, we simulated the acoustic radiation force for multiple wavelengths, pressure amplitudes, and *y*-axis positions, and for different *C. elegans* compressibility κ_{Ce} values. Note that the parameters d and e are specific to the specified *C. elegans* geometry. The *C. elegans* geometry was parametrized using its diameter and length, which were measured in the experiments. To avoid singularities, the ends of the cylinder were rounded in the scattering simulation (see Supporting Materials and Methods, Section 8).

The complete simulations for all *C. elegans* in our experiments ($n = 30$) took ~7 h by using the discretization described in Supporting Materials and Methods, Section 8. Once we obtained the parameters d and e for each worm, the acoustic radiation force could be readily calculated using the function f_{lin} as a function of pressure amplitudes, wavelengths, positions, and *C. elegans* compressibilities (Fig. 3 *c*). A time integration algorithm allowed us then to calculate the velocities $v_{ind,s}$ (Fig. 3 *d*). We then obtained the pressure amplitudes p_a from the PTV experiments and the indicator velocity values $v_{ind,e}$ for each of the worms from the WTV experiments (Fig. 3 *e*). Finally, we determined the compressibility of *C. elegans* κ_{Ce} that provides the best agreement between $v_{ind,s}$ and $v_{ind,e}$ using κ_{Ce} as fitting parameter.

RESULTS AND DISCUSSION

In situ determination of *C. elegans* acoustic compressibility κ_{Ce}

In the following, the results for the determination of the compressibility κ_{Ce} are presented, including the WTV
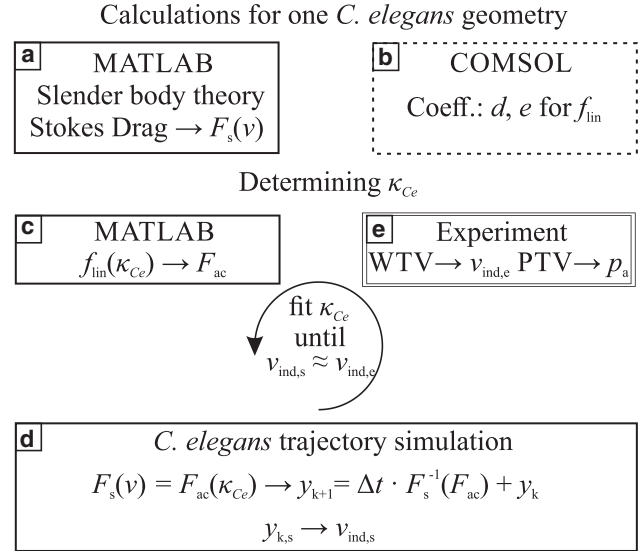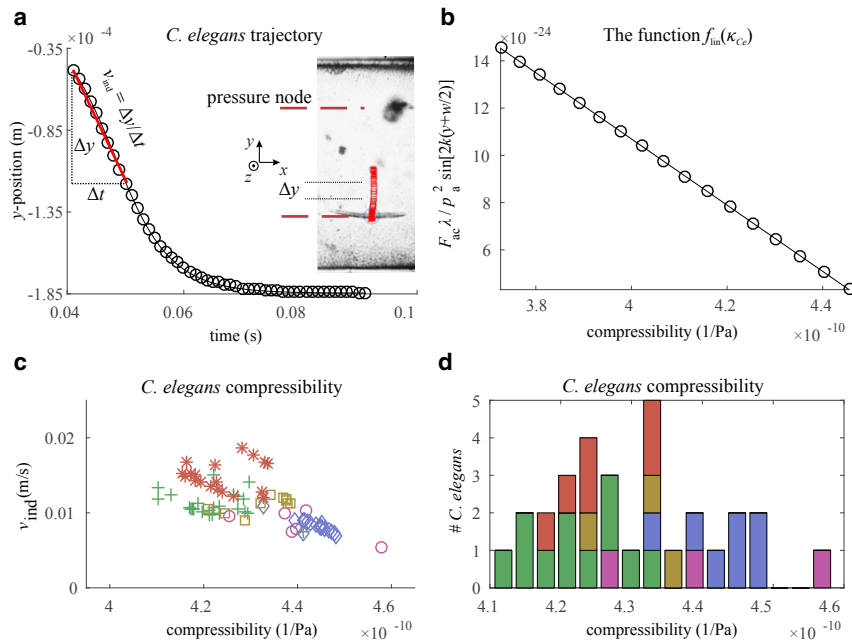
FIGURE 3 Flowchart for determining the *C. elegans* compressibility κ_{Ce}. The solid framed panels are performed using MATLAB, the dashed framed panel is done using COMSOL, and the double framed panel is obtained from experimental data. (*a*) The slender body theory is used to estimate the drag coefficients of a *C. elegans* between two parallel walls. (*b* and *c*) COMSOL is used to acquire the coefficients d and e of f_{lin}, which are subsequently used to calculate the acoustic radiation force acting on a *C. elegans*. (*d*) Given f_{lin}, we can calculate *C. elegans* trajectory and velocity $v_{ind,s}$ by balancing the Stokes' drag force F_s and the acoustic radiation force F_{ac} as a function of *C. elegans* compressibility κ_{Ce}. (*e*) From the velocimetry experiments, we obtain the pressure amplitudes p_a and the experimentally observed indicator velocity of the worms $v_{ind,e}$. The *C. elegans* compressibility is estimated by minimizing the difference between the calculated $v_{ind,s}$ and the experimentally observed $v_{ind,e}$.

experiment of Levamisole-paralyzed N2 L1 *C. elegans* (with a length of $l = 255 \pm 26$ μm and a diameter of $d = 15 \pm 2$ μm) in a well-characterized device and the fitting of the *C. elegans* compressibility to the resulting data. In WTV experiments, the position data of *C. elegans* translating along the *y*-axis without orientation changes were recorded (see Fig. 4 *a*). Following the procedure described in Fig. 3, we estimated the compressibility κ_{Ce} for each individual worm by fitting the simulated worm indicator velocity $v_{ind,s}$ to the experimental indicator velocity $v_{ind,e}$. Fig. 4 *a* shows an example of one numerical trajectory (*solid line*) and the corresponding experimental trajectory (*circular markers*) after fitting the indicator velocities. Fig. 4 *b* shows an example of 17 a priori scattering simulations for a *C. elegans* of 20 μm in diameter and a length of 291 μm. For the simulations we varied the pressure amplitude, wavelength, and worm compressibility in the equally spaced intervals of 0.5–3 MPa, 700–1400 μm, and 370–450 TPa^{-1}, respectively, and the worm was always placed at a distance of $\lambda/8$ away from the pressure node. The circular markers represent a single scattering simulation for one single geometry and for each simulation we used a specific combination of

FIGURE 4 For a Figure360 author presentation of Figure360▷
Fig. 4, see the figure legend at https://doi.org/10.1016/j.bpj.2018.08.048#mmc4.
Determination of *C. elegans* compressibility. (*a*) An example trajectory of a Levamisole-treated *C. elegans* is shown. The dots mark points obtained in the experiment, and the solid line gives the best fit from the numerical simulation. Starting from the position along the pressure nodal line of the $\lambda/2$-mode, *C. elegans* migrated toward the side of the channel upon switching to the λ-mode. The pressure nodal lines of the λ-mode are marked by red dashes and red rectangles in the inset mark trajectory points. (*b*) The function *f* from Eq. 4 is approximated as a linear function of the worm compressibility: $f_{\text{lin}} = d\kappa_{Ce} + e$. To determine the constants *d* and *e*, the acoustic radiation force F_{ac} was simulated for 17 different combinations of wavelength λ, pressure amplitude p_a, position *y*, and *C. elegans* compressibilities κ_{Ce}. The factors *d* and *e* were determined from this graph using a least square regression method. (*c* and *d*) The compressibility of a *C. elegans* was estimated by a one parameter fit of the model simulation to the experimental velocity $v_{\text{ind,e}}$. (*c*) The worm compressibilities estimated from 76 trajectories, corresponding to 30 different *C. elegans*. The different markers and colors correspond to five different measurement sessions. (*d*) The distribution of worm compressibilities for 30 different *C. elegans*. The compressibility of each *C. elegans* is averaged over the values from multiple trajectories. The average compressibility of the 30 *C. elegans* is 430 TPa^{-1}, whereas the SD is 11 TPa^{-1}. The spread of the data can be explained by the possible small variation in the internal morphology of our used *C. elegans*. Summing the main uncertainty contributions, i.e., the uncertainties due to the density variation, the choice of the segment when determining the indicator velocity and the SD from the experiments, we obtain a total uncertainty range of ± 20 TPa^{-1}. The colors in the bar plot in (*d*) correspond to the colors in the scatter plot in (*c*).

the four parameters: pressure amplitude, wavelength, worm compressibility, and worm position. The line represents the linear regression function f_{lin}. The parameters *d* and *e* are the slope and *y*-intercept of the linear regression function f_{lin}, respectively. The parameters *d* and *e* were evaluated for each of the 30 different worm geometries individually. We calculated the mean R-squared value for our 30 fits and obtained a value of 0.999999989876.

We collected data over the course of five independent measurement sessions, totaling 30 *C. elegans* and 76 WTV trajectories. For each *C. elegans* trajectory, we computed the experimentally observed v_{ind} and obtained the best value of worm compressibility following the procedure described in Fig. 3. The estimated worm compressibility values for each of the 76 trajectories are shown in Fig. 4 *c*. Different measurement sessions are represented by different markers and colors in the scatter plot. The distribution of averaged compressibility of the 30 *C. elegans*—averaged over multiple trajectories of each worm—are summarized in the bar plot in Fig. 4 *d*. From the distribution, we determined the average compressibility of the worms to be 430 TPa^{-1} and the SD to be 11 TPa^{-1}. Throughout our work, we used a density value of 1075 kg/m^3 for the computations. To estimate the uncertainty, we performed the simulation with density values of 1070 and 1080 kg/m^3 and obtained a ratio $\Delta\kappa/\Delta\rho$ of 0.4 TPa^{-1} m^3 kg^{-1}. This adds an additional uncertainty

of ± 2 TPa^{-1} to our final compressibility result, as our density value is 1075 $\pm$ 5 kg/m^3. Combining the main contributions to the uncertainty, i.e., the uncertainties due to the choice of the segment when determining the indicator velocity, the uncertainty due to density variations and the SD obtained from the experiments, and rounding to two significant figures, we obtain a compressibility value of 430 TPa^{-1} with an uncertainty range of ± 20 TPa^{-1}. The uncertainty range of 20 TPa^{-1} is in a typical magnitude for acoustofluidic compressibility measurements, as shown in Table 1. A comparison to compressibility measurements of sedimented *C. elegans* without applying the levitation in *z*-direction is given in Supporting Materials and Methods, Section 9.

Our results suggest that the acoustic compressibility of the *C. elegans* is very close to that of water ($\kappa_w = 444$ TPa^{-1}). Our estimated values for the compressibility of *C. elegans* differed by several orders of magnitude from those obtained by Gilpin et al. (14) ($\kappa_{Ce,S} = 625–833 \times 10^4$ TPa^{-1}). Gilpin et al. measured the compressibility of *C. elegans* under the influence of a static pressure, giving the worms enough time to adapt to the external pressure changes. Similar to work on the acoustic compressibility on individual cancer cell lines (33), in our study we were interested in the acoustic compressibility in the MHz regime. At this frequency, the living cells or organisms are unable to physiologically or physically react and/or adapt by releasing water or changing osmolality.

TABLE 1 Summary of Relevant Material Properties for Comparison

Material Group	Specimen	ρ [kg/m³]	c [m/s]	κ [1/TPa]	Ref.
Water		1000	1500	444.4[a]	(50,51)
Tissue	mean value for mammals[b]	1050	1577	380–383[a]	(52)
	brain (mammals)	1032 ± 6	~1562	395–399[a]	(52)
	liver (mammals)	1055 ± 12	~1585	373–382[a]	(52)
	muscle (mammals)	1058 ± 8	~1585	373–379[a]	(52)
	human myocardium (collagen)	1050	1530–1550	396–407[a]	(53)
	skin (epidermis/dermis)	1020 est.	1620	374[a]	(54,55)
	fat (mammals)	928 ± 3	~1457	506–509[a]	(52,56)
Cells	red blood cell	1099 ± 4, 1084 ± 1	–	331 ± 2, 336–348	(40,57–59)
	NIH/3T3 fibroblast	1079	–	378 ± 17	(40,60)
	MCF-12A (normal breast cell)	1068	–	377 ± 9	(40,61,62)
	MCF-7 breast cancer cell	1068	–	422 ± 9, 380 ± 30	(33,40,61)
	MDA breast cancer cell	–	–	430 ± 20	(33)
C. elegans	static, $\kappa_{Ce,S}$	–	–	(625–833) × 10⁴[a]	(14)
	acoustic, κ_{Ce}	1075 ± 5	–	430 ± 20	–

[a]κ is calculated from ρ and c.
[b]Mean value for the speed of sound for kidney, heart and skeleton muscle, spleen, and brain for mammals (young cattle, pig, horse, and human).

Notably, our estimated *C. elegans* compressibility values are within the same order of magnitude as the values reported for cells and bulk tissue samples. This agreement gives support that our measurement technique is applicable to living organisms. The previously reported and calculated compressibilities for bulk tissue (excluding fat) and individual cells indicate that for the majority of normal tissues and cells, the compressibility value is ~385 TPa⁻¹ (see Table 1). Aberrant cancerous cell lines have slightly increased compressibilities, which are in the same range as the values we obtained for *C. elegans*. Whereas the increased κ for cancerous cell lines is likely induced by substantial changes in the intracellular architecture (cytoskeleton), we attribute the higher compressibility of *C. elegans* to a higher fraction of water and adipose tissue (fat storage vesicles and membrane rich organs) throughout the cross-section of the *C. elegans* body than the average normal tissues or cells. To a first approximation, the *C. elegans* body composition can be divided into three major components: biological tissue material, water (mainly in the pseudocoelomic cavity and intestinal lumen), and adipose tissue in the inner section (see Supporting Materials and Methods, Section 10). As shown in Table 1, the compressibility of water and fat tissue is generally higher than that of other cells and tissues, including cancerous cells. Ellenby (34) determined the overall water content of *Panagrellus redivivus* nematodes by interference microscopy. A nematode in its larval stage has a water content of 80% and a cell solid content of 20%. Hellerer et al. (35) determined a relative volume fraction of fat containing lipid droplets in wild-type L4 *C. elegans* to be 17 ± 5%. For a mutant dauer larvae, the lipid content increased to 27 ± 5%.

Previous studies on the acoustophoretic behavior of composite spheres demonstrated that the acoustophoretic mobility follows a simple linear "mixing rule," relating the compressibility of a particle to the relative volume fractions of materials comprising the particle (36,37). Assuming

that *C. elegans* consists of water, tissue and/or cells (i.e., ~385 TPa⁻¹) and fat (in membranous form or in storage droplets, etc., ~508 TPa⁻¹), the *C. elegans* compressibility can be expressed as a function of the compressibility of each of the components, as follows:

$$\kappa_{Ce} \approx -\frac{1}{V_{tot}}\frac{\partial\left(V_w + V_f + V_t\right)}{\partial p} = \frac{1}{V_{tot}}\left(V_w\kappa_w + V_f\kappa_f + V_t\kappa_t\right),$$

(6)

where V_w (κ_w), V_t (κ_t), and V_f (κ_f) denote the volume fractions (compressibilities) of water, tissues and/or cells, and fat, respectively. By assuming a high water content for our *C. elegans* larvae, we assigned the composition of *C. elegans* to 50% water, 40% tissue and/or cells, and 10% fat (volumetric fraction). Using the compressibility values for each of these components from Table 1 (i.e., $\kappa_w = 444$ TPa⁻¹, $\kappa_t = 385$ TPa⁻¹, $\kappa_f = 508$ TPa⁻¹) and the mixing rule above, we obtained a compressibility value of 421 TPa⁻¹, which is close to our measured compressibility for the *C. elegans*. The compressibility of the *C. elegans* cuticle has not been reported in the literature but might be comparable to epidermal tissue (see Table 1). However, the contribution of the *C. elegans* cuticle to the compressibility in the case of L1 is expected to be comparatively small since the cuticle contributes only 0.2 μm to the 8 μm radius of a L1 *C. elegans* (see Fig. S7 *b*). In contrast to the method by Rigato et al. (38), who used an atomic force microscope tip to measure local mechanical properties, our acoustic method results in a compressibility of the overall average body composition. It is not possible to measure a local compressibility of e.g. single filaments for a direct comparison to the results of Rigato et al. (38). Thus, our measured compressibility value is in the same order of magnitude as a homogeneous clump of mixed cellular material.

Although we prepared the worms as uniformly as possible among different experimental days, there exists batch-to-batch variability in the worm dimensions. Such variability could arise from differences in the age of the worms. As previously noted by Fouad et al. (39), the fat content of *C. elegans* increases quickly between L1 and L2. According to the mixing rule in Eq. 6, a higher fat content in the larger (and presumably older) worms should correspond to higher compressibility. As shown in Fig. S8 (see Supporting Materials and Methods, Section 11), larger worms, particularly in diameter, have higher compressibility values, which is in agreement with the above expectation.

CONCLUSION

The overall compressibility of a biological specimen is an informative parameter within the context of biophysical research (40,41). For this purpose, we rigorously established an efficacious procedure for determining the overall acoustic compressibility in the MHz range of a widely used model organism, *C. elegans*. By balancing the Stokes' drag and acoustic radiation forces using two simulation approaches, we determined the compressibility of L1 *C. elegans*. We provided a computationally efficient and accurate procedure for the compressibility estimation, which could readily take into account different L1 *C. elegans* dimensions. We determined the compressibility of an average L1 *C. elegans* to be $\kappa_{Ce} = 430 \text{ TPa}^{-1}$, with an uncertainty range of $\pm 20 \text{ TPa}^{-1}$. Our results further suggest that the acoustic behavior can be computed based on the average body composition using a "mixing rule," as reported in (36,37). Thus, our acoustic method of determining the *C. elegans* compressibility might also be useful in the future to provide a combined platform-technique for the body composition of *C. elegans* at different developmental stages. Additionally, our approach is not limited to *C. elegans* and may also be applied to determine the compressibility of other nonspherical biological specimens such as bacteria and protozoan pathogens.

SUPPORTING MATERIAL

Supporting Materials and Methods, eight figures, one table, and two videos are available at http://www.biophysj.org/biophysj/supplemental/S0006-3495(18)31068-3.

AUTHOR CONTRIBUTIONS

P.R., T.B., and J.D. developed the experimental design. S.L., P.R., and T.B. established the idea to systematically determine the compressibility. P.R. and G.H. fabricated the devices. T.B. performed the numerical work. N.V.-Q. cultured and prepared *C. elegans*. P.R., T.B., N.V.-Q., and S.L. performed the experiments. P.R. and T.B. analyzed data. P.R., T.B., and S.L. discussed and prepared figures and manuscript. J.D. provided overall guidance and contributed to the experimental design. S.L., T.B., P.R., and N.V.-Q. wrote the manuscript with critical reading by X.C.i.S., R.G., A.de., and J.D. All the authors contributed to the scientific discussion in the process of manuscript revision. The initial collaboration rooted in a dis-

cussion of how to use acoustics to position *C. elegans* in microfluidic high-throughput analysis channels between N.V.-Q., P.R. and further Institute of Mechanical Systems PhD students, X.C.i.S., J.D., and R.G., sparked by R.G. during an Eidgenössische Technische Hochschule Zürich Strategy meeting.

ACKNOWLEDGMENTS

SUPPORTING CITATIONS

References (42–49) appear in the Supporting Material.

REFERENCES

1. Dittrich, P. S., K. Tachikawa, and A. Manz. 2006. Micro total analysis systems. Latest advancements and trends. *Anal. Chem.* 78:3887–3908.

2. Haeberle, S., and R. Zengerle. 2007. Microfluidic platforms for lab-on-a-chip applications. *Lab Chip.* 7:1094–1110.

3. Christakou, A. E., M. Ohlin, …, M. Wiklund. 2015. Ultrasonic three-dimensional on-chip cell culture for dynamic studies of tumor immune surveillance by natural killer cells. *Lab Chip.* 15:3222–3231.

4. Wiklund, M. 2012. Acoustofluidics 12: biocompatibility and cell viability in microfluidic acoustic resonators. *Lab Chip.* 12:2018–2028.

5. Park, J. W., S. H. Kim, …, K. Goda. 2016. Acoustofluidic harvesting of microalgae on a single chip. *Biomicrofluidics.* 10:034119.

6. Saito, M., N. Kitamura, and M. Terauchi. 2002. Ultrasonic manipulation of locomotive microorganisms and evaluation of their activity. *J. Appl. Phys.* 92:7581–7586.

7. Schwarz, T. 2013. Rotation of particles by ultrasonic manipulation. PhD thesis (Eidgenössische Technische Hochschule ETH Zürich).

8. Barr, M. M. 2003. Super models. *Physiol. Genomics.* 13:15–24.

9. Cornaglia, M., T. Lehnert, and M. A. M. Gijs. 2017. Microfluidic systems for high-throughput and high-content screening using the nematode Caenorhabditis elegans. *Lab Chip.* 17:3736–3759.

10. Ahmed, D., A. Ozcelik, …, T. J. Huang. 2016. Rotational manipulation of single cells and organisms using acoustic waves. *Nat. Commun.* 7:11085.

11. Ding, X., S. C. Lin, …, T. J. Huang. 2012. On-chip manipulation of single microparticles, cells, and organisms using surface acoustic waves. *Proc. Natl. Acad. Sci. USA.* 109:11105–11109.

12. Yu, G., X. Chen, and J. Xu. 2011. Acoustophoresis in variously shaped liquid droplets. *Soft Matter.* 7:10063–10069.

13. Reina, A., A. B. Subramaniam, …, G. M. Whitesides. 2013. Shifts in the distribution of mass densities is a signature of caloric restriction in Caenorhabditis elegans. *PLoS One.* 8:e69651.

14. Gilpin, W., S. Uppaluri, and C. P. Brangwynne. 2015. Worms under pressure: bulk mechanical properties of C. elegans are independent of the cuticle. *Biophys. J.* 108:1887–1898.

15. Barnkob, R., P. Augustsson, …, H. Bruus. 2010. Measuring the local pressure amplitude in microchannel acoustophoresis. *Lab Chip.* 10:563–570.

16. Hahn, P., I. Leibacher, …, J. Dual. 2015. Numerical simulation of acoustofluidic manipulation by radiation forces and acoustic streaming for complex particles. *Lab Chip.* 15:4302–4313.

17. Brenner, S. 1974. The genetics of Caenorhabditis elegans. *Genetics.* 77:71–94.

18. Altun, Z., and D. Hall. 2015. Handbook of C. elegans Anatomy, WormAtlas. http://www.wormatlas.org.

19. Baugh, L. R. 2013. To grow or not to grow: nutritional control of development during Caenorhabditis elegans L1 arrest. *Genetics.* 194:539–555.

20. Gatzen, H. H., V. Saile, and J. Leuthold. 2015. Micro and Nano Fabrication. Springer, Berlin, Germany.

21. Leibacher, I., P. Reichert, and J. Dual. 2015. Microfluidic droplet handling by bulk acoustic wave (BAW) acoustophoresis. *Lab Chip.* 15:2896–2905.

22. Lamprecht, A., S. Lakämper, …, J. Dual. 2016. Imaging the position-dependent 3D force on microbeads subjected to acoustic radiation forces and streaming. *Lab Chip.* 16:2682–2693.

23. Lakämper, S., A. Lamprecht, …, J. Dual. 2015. Direct 2D measurement of time-averaged forces and pressure amplitudes in acoustophoretic devices using optical trapping. *Lab Chip.* 15:290–300.

24. Laurell, T., and A. Lenshof. 2014. Microscale Acoustofluidics. Royal Society of Chemistry, Cambridge, UK.

25. Yosioka, K., and Y. Kawasima. 1955. Acoustic radiation pressure on a compressible sphere. *Acta Acust. United Acust.* 5:167–173.

26. Kundu, P., I. Cohen, and D. Dowling. 1990. Low reynolds number viscous flow past a sphere. *In* Fluid Mechanics, Fifth edition. Academic Press, Cambridge, MA, pp. 338–347.

27. Kanaris, N., D. Grigoriadis, and S. Kassinos. 2011. Three dimensional flow around a circular cylinder confined in a plane channel. *Phys. Fluids.* 23:064106.

28. Barnkob, R. 2012. Physics of microparticle acoustophoresis: bridging theory and experiment. PhD thesis (DTU Nanotech, Technical University of Denmark).

29. Faxén, H. 1922. Der Widerstand gegen die Bewegung einer starren Kugel in einer zähen Flüssigkeit, die zwischen zwei parallelen ebenen Wänden eingeschlossen ist. *Ann. Phys.* 373:89–119.

30. De Mestre, N. 1973. Low-Reynolds-number fall of slender cylinders near boundaries. *J. Fluid Mech.* 58:641–656.

31. Barnkob, R., P. Augustsson, …, H. Bruus. 2012. Acoustic radiation- and streaming-induced microparticle velocities determined by microparticle image velocimetry in an ultrasound symmetry plane. *Phys. Rev. E Stat. Nonlin. Soft Matter Phys.* 86:056307.

32. Burri, M., T. Baasch, and P. Reichert. 2017. GUI for the characterization of acoustofluidic devices (v1.7). MathWorks File Exchange.

33. Yang, T., F. Bragheri, …, P. Minzioni. 2016. A comprehensive strategy for the analysis of acoustic compressibility and optical deformability on single cells. *Sci. Rep.* 6:23946.

34. Ellenby, C. 1968. Determination of the water content of nematode worms by interference microscopy. *Experientia.* 24:84–85.

35. Hellerer, T., C. Axäng, …, A. Enejder. 2007. Monitoring of lipid storage in Caenorhabditis elegans using coherent anti-Stokes Raman scattering (CARS) microscopy. *Proc. Natl. Acad. Sci. USA.* 104:14658–14663.

36. Leibacher, I., W. Dietze, …, J. Dual. 2014. Acoustophoresis of hollow and core-shell particles in two-dimensional resonance modes. *Microfluid. Nanofluidics.* 16:513–524.

37. Hashin, Z. 1962. The elastic moduli of heterogeneous materials. *J. Appl. Mech.* 29:143–150.

38. Rigato, A., A. Miyagi, …, F. Rico. 2017. High-frequency microrheology reveals cytoskeleton dynamics in living cells. *Nat. Phys.* 13:771–775.

39. Fouad, A. D., S. H. Pu, …, C. Fang-Yen. 2017. Quantitative assessment of fat levels in Caenorhabditis elegans using dark field microscopy. *G3 (Bethesda).* 7:1811–1818.

40. Hartono, D., Y. Liu, …, K. M. Lim. 2011. On-chip measurements of cell compressibility via acoustic radiation. *Lab Chip.* 11:4072–4080.

41. Wang, H., Z. Liu, …, A. Han. 2013. Acoustophoretic force-based compressibility measurement of cancer cells having different metastatic potential. *In* Proceedings of Meetings on Acoustics. Acoustical Society of America.

42. Bridgman, W. B. 1942. Some physical chemical characteristics of glycogen. *J. Am. Chem. Soc.* 64:2349–2356.

43. Pertoft, H., T. C. Laurent, …, L. Kågedal. 1978. Density gradients prepared from colloidal silica particles coated by polyvinylpyrrolidone (Percoll). *Anal. Biochem.* 88:271–282.

44. 2001. Percoll: methodology and applications. Amersham Biosciences, Little Chalfont, United Kingdom.

45. Morley, J. F., and R. I. Morimoto. 2004. Regulation of longevity in Caenorhabditis elegans by heat shock factor and molecular chaperones. *Mol. Biol. Cell.* 15:657–664.

46. Corsi, A. K., B. Wightman, and M. Chalfie. 2015. A transparent window into biology: a primer on Caenorhabditis elegans. *WormBook* 1–31.

47. Oberti, S. 2009. Micromanipulation of small particles within micromachined fluidic systems using ultrasound. PhD thesis (Eidgenössische Technische Hochschule ETH Zürich).

48. Mobley, J., C. S. Hall, …, J. G. Miller. 1999. Measurements and predictions of the phase velocity and attenuation coefficient in suspensions of elastic microspheres. *J. Acoust. Soc. Am.* 106:652–659.

49. Johnstone, I. L. 1994. The cuticle of the nematode Caenorhabditis elegans: a complex collagen structure. *BioEssays.* 16:171–178.

50. Selfridge, A. R. 1985. Approximate material properties in isotropic materials. *IEEE Trans. Sonics Ultrason.* 32:381–394.

51. Lemmon, E. 2011. Thermophysical properties of water and steam. *In* CRC Handbook of Chemistry and Physics. CRC Press.

52. Frucht, A.-H. 1953. Die Schallgeschwindigkeit in menschlichen und tierischen Geweben. *Zeitschrift für Die Gesamte Experimentelle Medizin.* 120:526–557.

53. Hoffmeister, B. K., E. D. Verdonk, …, J. G. Miller. 1994. Effect of collagen on the anisotropy of quasi-longitudinal mode ultrasonic velocity in fibrous soft tissues: a comparison of fixed tendon and fixed myocardium. *J. Acoust. Soc. Am.* 96:1957–1964.

54. Liang, X., and S. A. Boppart. 2010. Biomechanical properties of in vivo human skin from dynamic optical coherence elastography. *IEEE Trans. Biomed. Eng.* 57:953–959.

55. Moran, C. M., N. L. Bush, and J. C. Bamber. 1995. Ultrasonic propagation properties of excised human skin. *Ultrasound Med. Biol.* 21:1177–1190.

56. Fidanza, F., A. Keys, and J. T. Anderson. 1953. Density of body fat in man and other mammals. *J. Appl. Physiol.* 6:252–256.

57. Leif, R. C., and J. Vinograd. 1964. The distribution of buoyant density of human erythrocytes in bovine albumin solutions. *Proc. Natl. Acad. Sci. USA.* 51:520–528.

58. Weiser, M. A. H., and R. E. Apfel. 1982. Extension of acoustic levitation to include the study of micron-size particles in a more compressible host liquid. *J. Acoust. Soc. Am.* 71:1261–1268.

59. Shung, K. K., B. A. Krisko, and J. O. Ballard, III. 1982. Acoustic measurement of erythrocyte compressibility. *J. Acoust. Soc. Am.* 72:1364–1367.

60. Manoussaka, M. S., D. J. Jackson, …, B. M. Kumpel. 2005. Flow cytometric characterisation of cells of differing densities isolated from human term placentae and enrichment of villous trophoblast cells. *Placenta.* 26:308–318.

61. Griwatz, C., B. Brandt, …, K. S. Zänker. 1995. An immunological enrichment method for epithelial cells from peripheral blood. *J. Immunol. Methods.* 183:251–265.

62. Brandt, B., C. Griwatz, …, K. S. Zänker. 1996. Detection of the metastatic potential of blood-borne and immunomagnetically enriched epithelial cells by quantitative erbB-2 RT-PCR. *Clin. Exp. Metastasis.* 14:399–408.